Tunable valley-spin splitting in a Janus XMSiN$_2$ monolayer (X = S, Se; M = Mo, Cr) and giant valley polarization via vanadium doping

Jun Zhao [1,*] Yunxi Qi,[1] Can Yao,[1] and Hui Zeng [2,†]

[1]*New Energy Technology Engineering Laboratory of Jiangsu Province & School of Science, Nanjing University of Posts and Telecommunications, Nanjing, Jiangsu 210023, China*

[2]*School of Microelectronics, Nanjing University of Science and Technology, Nanjing, Jiangsu 210094, China*

Exploring spin-valley coupling in two-dimensional (2D) materials with strong spin-orbit coupling (SOC) is of great significance for fundamental physics and practical applications. Using first-principles calculations, we investigate the valley-related properties of Janus XMSiN$_2$ (X=S, Se; M=Mo, Cr) monolayer. The Janus XMSiN$_2$ monolayer forms a pair of nonequivalent valleys, and the conduction and valence bands are degenerated at the valleys. The inversion symmetry breaking and the SOC effect induce remarkable valley spin splitting and Rashba spin splitting. Our calculations indicate that not only valley-contrasting transport properties but also optical selection rules with spin-valley coupling result in the coexistence of spin and valley Hall effects in the Janus XMSiN$_2$ monolayer. Moreover, we demonstrate that the valley-spin physics of the Janus XMSiN$_2$ monolayer can be modulated by in-plane biaxial strains, allowing its extraordinary potential for spintronics and valleytronic applications. We also show that V-doped SMoSiN$_2$ monolayer can exhibit giant valley polarization of 89.51 meV (-24.48 meV) for the valence (conduction) band. These findings could be helpful for the valleytronic applications of the Janus XMSiN$_2$ monolayer.

I. INTRODUCTION

Recently, a new class of 2D materials, named Janus 2D monolayers, has attracted extensive attentions [1,2]. Owing to the mirror symmetry breaking, the 2D Janus structure exhibits excellent properties such as in-plane anisotropy, valley spin splitting, Rashba spin splitting, out-of-plane piezoelectric polarization, and photocatalysis [3–6]. For example, the asymmetric crystal potential causes the intrinsic electric field in Janus 2D materials such as WSiGeN$_4$, Si$_2XY$ ($X, Y =$ P, As, Sb, and Bi), and both valley-related spin splitting and Rashba spin splitting can be obtained [7,8]. In addition, Dong *et al.* reported that the piezoelectric properties of Janus monolayers can be substantially higher than those of commonly used monolayered materials [9]. Previous results showed that both strains and vacancy defects can make the Janus MoSSe monolayer superior to the pristine MoS$_2$ or MoSe$_2$ in hydrogen evolution reactions (HER) [10,11].

The development of 2D Janus materials has also brought impetus to many other fields, such as valleytronics [12–14]. In analogy to charge and spin, valley is regarded as a novel degree of freedom and can be used for information encoding and processing [15]. Owing to the separation of the valley in momentum space, phonon scattering between different valleys is prohibited. Therefore materials with outstanding valley properties are promising for electronic devices with high storage density and low energy consumption [12,16]. Many Janus 2D materials have spin-valley locking and opposite Berry curvatures at K and K' valleys due to inversion symmetry breaking and strong SOC [10,17–20]. Previous theoretical predictions of valley Hall effect, spin Hall effect, and valley-dependent optical selection rules have recently been verified by experimental measurements [21–25]. Exploring novel 2D Janus semiconductors and discovering more 2D Janus material platforms to achieve valley-related properties are crucial for potential applications of valleytronic devices.

More recently, Sibatov *et al.* have proposed the Janus SMoSiN$_2$ monolayer with five layers of atoms, which can be obtained from MoSi$_2$N$_4$ by replacing N-Si-N atoms on one side with S atoms [26]. These monolayers can be regarded as 2D Janus materials with mirror symmetry breaking, which produces some extraordinary properties. The calculated results demonstrate that these XMSiN$_2$ (X=S, Se, Te; M=Mo, Cr) monolayers are dynamically and thermodynamically stable, and they are semiconductors with band gaps of about 1–3 eV, making them promising candidates for nanoelectronics and photovoltaics [27,28]. The first-principles calculation predicted the formation of tunable Schottky contact at the graphene/Janus SMoSiN$_2$ interface [29], in analogy to the case of graphene/C$_3$N heterostructure [30], facilitating nanoelectronic application of the Janus SMoSiN$_2$-based nanomaterials. Feng *et al.* reported the bias-dependent spin filtering effect and temperature-driven spin Seebeck effect in the VSi$_2$P$_4$ monolayer [31]. However, the explorations of versatile properties of 2D Janus nanostructures based on MA_2Z_4 (M=Cr, Mo, W, V, Nb, Ta, Ti, Zr or Hf; A=Si or Ge; and Z=N, P, As) family are still lacking [32,33].

In this work, utilizing first-principles calculations, we demonstrate that the Janus XMSiN$_2$ (X=S, Se; M=Mo, Cr) monolayers with remarkable valley-contrasting physics are

*zhaojun@njupt.edu.cn
†zenghui@njust.edu.cn

promising candidates for valleytronics. These monolayers are all semiconductors with unequal valleys at K and K' points. The Rashba splitting induced by inversion symmetry breaking is observed. In addition, our calculation reveal that both optical absorption and valley spin splitting of the Janus $XM\mathrm{SiN}_2$ can be manipulated by biaxial tensile strains. We further predict that giant valley polarization of SMoSiN_2 can be generated by doping. Our investigations provide physical insights into the modulation of valley-related properties of the Janus $XM\mathrm{SiN}_2$ monolayers, facilitating their potential applications for spintronics, valleytronics, and related devices.

II. COMPUTATIONAL DETAILS

The band structures, density of states, and optical properties of materials are calculated in the Vienna *ab initio* simulation package (VASP) based on density functional theory [34]. The ionic potential is described by the projection augmented wave (PAW) method [35]. The exchange and correction interaction is characterized by the Perdew-Burke-Ernzerhof (PBE) functional of the generalized gradient approximation (GGA) [36]. The energy cut-off of the plane wave basis is 500 eV. The convergence criteria for total energy and residual atomic force are 1×10^{-8} eV and 0.01 eV/Å, respectively. To avoid artificial interactions between periodic images, a vacuum distance of 20 Å is chosen. The Brillouin zone (BZ) is sampled by using a $16 \times 16 \times 1$ Γ-centered k-point grid for structural optimization and electronic structure calculation [37]. The dipole correction is considered in all calculations.

The optical absorption coefficient $\alpha(\omega)$ is computed by frequency-dependent dielectric function $\varepsilon(\omega)$ within the framework of linear response theory [38]:

$$\alpha(\omega) = \sqrt{2}\omega[\sqrt{\varepsilon_1(\omega)^2 + \varepsilon_2(\omega)^2} - \varepsilon_1(\omega)]^{\frac{1}{2}}, \qquad (1)$$

where $\varepsilon_1(\omega)$ and $\varepsilon_2(\omega)$ are the real and imaginary parts of the dielectric function, respectively. On the basis of Kramer-Kroning transformation [38], the real part $\varepsilon_1(\omega)$ can be obtained from the corresponding imaginary part. We thus concentrate on the computation of the imaginary part $\varepsilon_2(\omega)$:

$$\varepsilon_2(\omega) = \frac{4\pi^2 e^2}{\Omega} \lim_{q \to 0} \frac{1}{q^2} \Sigma_{c,v,k} 2W_k \delta(\epsilon_{ck} - \epsilon_{vk} - \omega)$$
$$\times \langle u_{ck+e_\alpha q}|u_{vk}\rangle \langle u_{ck+e_\beta q}|u_{vk}\rangle^*, \qquad (2)$$

where the indices c and v denote conduction and valence band states, respectively. Hence, the phonon dispersion calculations are performed by density functional perturbation theory, which is implemented by the PHONOPY code [39]. A $4 \times 4 \times 1$ supercell is used for the phonon dispersion calculation. The PYPROCAR code is used to draw band structures with spin polarization [40]. The VASPBERRY subroutine is used to calculate the Berry curvature and circular polarization [41]. In addition, the VASPKIT post-processing tool is employed to deal with the calculated results [42].
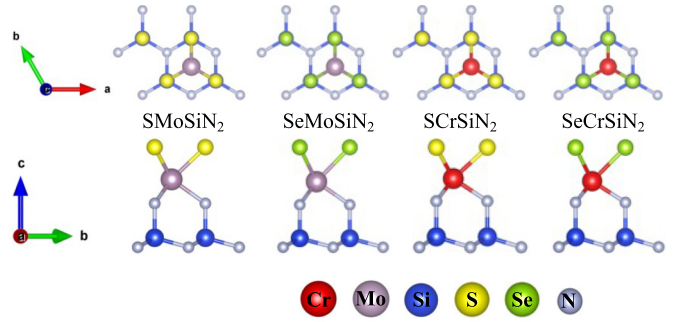
FIG. 1. Top and side views of the atomic structures of the $XM\mathrm{SiN}_2$ monolayers after structural optimization. The red, lavender, blue, yellow, green, and gray spheres representing Cr, Mo, Si, S, Se, and N atoms, respectively.

III. RESULTS AND DISCUSSION

A. Atomic structures and structural stabilities

The top and side views of the optimized crystal structure of $XM\mathrm{SiN}_2$ (X=S, Se; M=Mo, Cr) are shown in Fig. 1, in which the stacking of the atomic layers is X-M-N-Si-N. The atomically structural parameters of the monolayered $XM\mathrm{SiN}_2$ are summarized in Table I. It is found that the maximum lattice constant is 3.014 Å for the $\mathrm{SeMoSiN}_2$ monolayer, followed by SMoSiN_2 (2.980 Å), $\mathrm{SeCrSiN}_2$ (2.935 Å), and SCrSiN_2 (2.896 Å), which is consistent with previous reports [26,27]. The structural differences in lattice constant, bond length, and thickness are attributed to the different atomic radii of Mo, Cr, Se, and S atoms. Owing to the lack of inversion symmetry, the $XM\mathrm{SiN}_2$ monolayers are expected to possess many exotic properties, such as Rashba spin splitting and out-of-plane piezoelectric polarization. The dynamic stabilities of these Janus monolayers are examined by computing their phonon spectra. As shown in Fig. 2, no distinct imaginary frequency branches are observed. It suggests that the Janus $XM\mathrm{SiN}_2$ monolayers possess excellent stabilities, providing great possibilities for experimental synthesis and characterization in future.
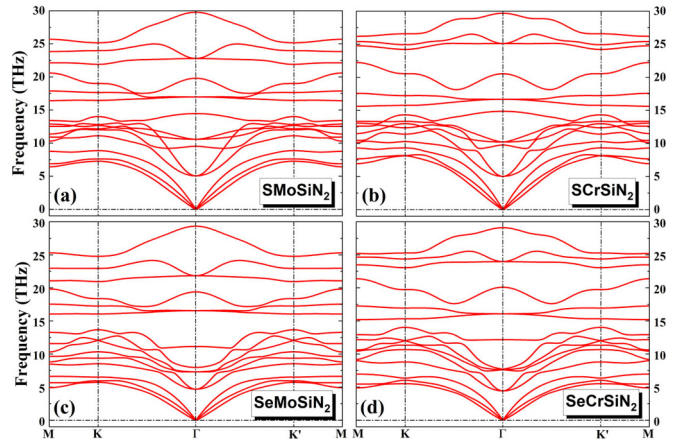
FIG. 2. The calculated phonon spectra for the (a) SMoSiN_2, (b) SCrSiN_2, (c) $\mathrm{SeMoSiN}_2$, and (d) $\mathrm{SeCrSiN}_2$ monolayers, respectively.

TABLE I. The lattice constants (a and b), shortest and longest Si-N bond length (R_{Si-N}), Mo/Cr-X bond length ($R_{Mo/Cr-X}$), thickness of monolayer (h), band gap without SOC (E_g^{PBE}) and with SOC ($E_g^{PBE+SOC}$), dipole moment per unit cell (P_y, P_z), and spin splitting energy of valence Δ_V and conduction band Δ_C of the XMSiN$_2$ monolayers.

	$a = b$ (Å)	R_{Si-N} (Å)	$R_{Mo/Cr-X}$	h (Å)	E_g^{PBE} (eV)	$E_g^{PBE+SOC}$ (eV)	P_y/P_z (e Å)	Δ_V (meV)	Δ_C (meV)
SMoSiN$_2$	2.980	1.75/1.79	2.38	5.10	2.15	2.06	2.15/0.0016	132.74	4.18
SCrSiN$_2$	2.896	1.75/1.75	2.27	4.91	0.79	0.79	1.84/0.0008	64.98	3.46
SeMoSiN$_2$	3.014	1.75/1.80	2.50	5.22	1.77	1.75	2.18/-0.0566	148.70	18.78
SeCrSiN$_2$	2.935	1.75/1.77	2.40	5.03	0.60	0.59	1.87/-0.0541	78.43	13.90

B. Electronic band structures

For the SMoSiN$_2$ monolayer, Figs. 3(a) and 3(b) shows that both valence band maximum (VBM) and conduction band minimum (CBM) are located at the K/K' valleys. Moreover, the energies at the K/K' valleys are degenerate. The SMoSiN$_2$ monolayer has a direct band gap of 2.15 eV when SOC effect is not taken into account. When the SOC effect is included, the degenerated VBM band is significantly lifted due to spin splitting. Figure 3(c) schematically demonstrates the spin splittings for both VBM and CBM at the K/K' valleys. The spin-up and spin-down states at the K/K' valleys are completely opposite, and the spin degree of freedom is locked with the valley index, leading to $E_K^{\uparrow} = E_{K'}^{\downarrow}$ [22]. Furthermore, the selectively optical transition is coupled with spin and governed by optical selection rule [12,43]. The electronic structure of the SCrSiN$_2$ monolayer shown in Figs. 3(d) and 3(e) reveals that it has an indirect band gap of 0.79 eV. Its CBM is in the vicinity of K/K' valleys, and its VBM is located at the Γ point.

Both SeMoSiN$_2$ and SeCrSiN$_2$ monolayers are indirect band gap semiconductors, as shown in Fig. 4. Because valleys are defined as the extreme points in the k space, Fig. 4 demonstrates that the valleys of the SeMoSiN$_2$ and SeCrSiN$_2$ monolayers almost vanish. In the following, we focus on the valley-related properties of the SMoSiN$_2$ and the SCrSiN$_2$ monolayers. To obtain a more accurate band-gap value, we use HSE06 [44] functional to compute the electronic band structures of the SMoSiN$_2$ and SCrSiN$_2$ monolayers, as shown in Fig. S1 [45]. The HSE06 band gaps of these two systems are found to be increased by 0.54 (0.55) eV compared to those obtained by PBE functional. Comparing Fig. 3 and Fig. S1, we find that the electronic orbital compositions, which are obtained by PBE and HSE06, are very similar. Considering extensive time consumption of the HSE06 calculation, we thus perform the valley-related calculations by GGA-PBE functional hereafter.

Moreover, according to the orbital-projected band structures, the K/K' valleys of the SMoSiN$_2$ and SCrSiN$_2$ monolayers are dominated by Mo-d and Cr-d orbitals, respectively. Figs. 3(a), 3(b) and 3(d), 3(e) show that the SOC effect did not change the characteristics of their band edges. The SMoSiN$_2$ (SCrSiN$_2$) monolayer is essentially a direct band-gap (indirect band-gap) semiconductor with 2.06 eV (0.79 eV) band gap. Specifically, the SMoSiN$_2$ monolayer is a most intriguing candidate for valleytronics since its direct band gap is exactly located at the K/K' valleys [46].
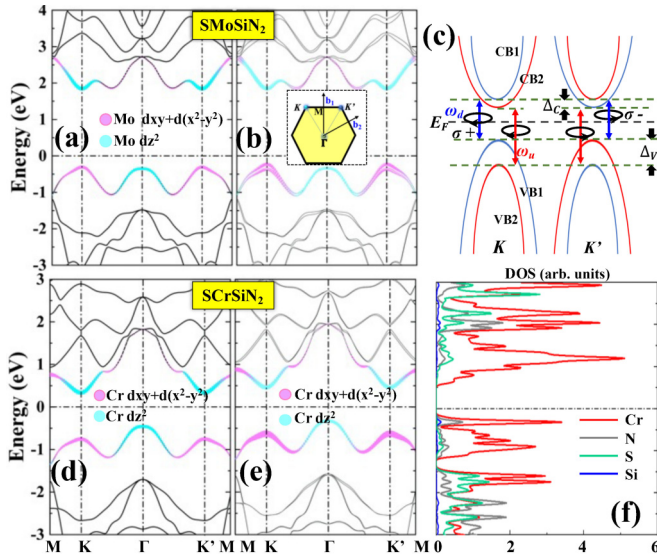
FIG. 3. The orbital-projected band structure of the SMoSiN$_2$ monolayer (a) without SOC and (b) with SOC. The Brillouin zone with some high-symmetry points is shown as a inset in (b). (c) Representation of valley spin splitting at the K/K' valleys and optical transitions, where the red and blue parabolas represent the spin-up and the spin-down bands, respectively. The red (ω_u) and blue (ω_d) arrows represent the minimal energies for spin-up and spin-down optical transitions at the K valley. The orbital-projected band structures of the SCrSiN$_2$ monolayer (d) without SOC and (e) with SOC. The (f) projected density of states (PDOS) of the SCrSiN$_2$ monolayer. The Fermi level E_F is set to 0.
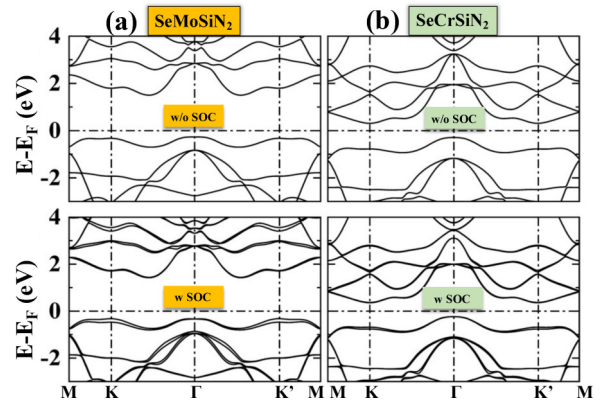
FIG. 4. The band structures of (a) the monolayered SeMoSiN$_2$ and (b) the monolayered SeCrSiN$_2$. The top and bottom figures refer to the calculated electronic structures without and with SOC, respectively.
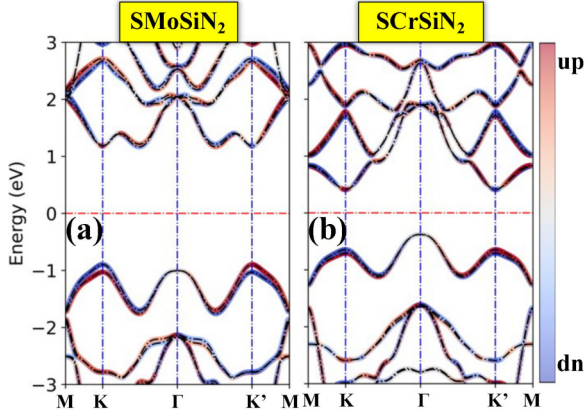
FIG. 5. The spin projected band structures of (a) the SMoSiN$_2$ and the (b) SCrSiN$_2$ monolayers with SOC. The color bars represent the weights of the spin component S_Z, and red (blue) is spin-up (spin-down) component.

C. Valley coupled spin splitting

The valley-related spin splitting for the valence and conduction bands are defined as $\Delta_V^{K/K'}$ and $\Delta_C^{K/K'}$, respectively. Owing to the protection of time reversal symmetry, Δ_V^K (Δ_C^K) is equal to $\Delta_V^{K'}$ ($\Delta_C^{K'}$). Therefore, as schematically shown in Fig. 3(c), the valley-related spin splitting is simplified to:

$$\Delta_V = E_K^{VB1} - E_K^{VB2} \left(\Delta_C = E_K^{CB1} - E_K^{CB2} \right) \qquad (3)$$

where E_K^{VB1} and E_K^{VB2} are the highest occupied band energy and the second highest occupied band energy at the K valley.

For the SMoSiN$_2$ and SCrSiN$_2$ monolayers, the top of the valence bands at the K/K' valley are completely spin polarized, as shown in Fig. 5. It suggests that the spin component S_Z is a good quantum number, and the suppressed Dyakonov-Perel spin relaxation can be obtained for both SMoSiN$_2$ and SCrSiN$_2$ monolayers [21]. The two valleys are connected by time reversal symmetry. The spin splittings of SMoSiN$_2$ and SCrSiN$_2$ monolayers at the valence band (Δ_V) are 132.74 and 64.98 meV, respectively. The corresponding values for the SeMoSiN$_2$ and SeCrSiN$_2$ monolayers are 148.70 and 78.43 meV, as summarized in Table I. The magnitude of Δ_V is determined by strength of SOC. For instance, compared to Cr and S atoms, Mo and Se atoms give rise to larger spin splitting. Our calculated spin-splitting values are similar to that of the MoS$_2$ ($\sim$150 meV) monolayer [47], MoSi$_2$P$_4$ (139.4 meV) monolayer [48], and CrSiGeN$_4$ (63 meV) monolayer [49]. The large valley-coupled spin splitting obtained for the SMoSiN$_2$ monolayer can establish robust valley-spin coupling, which is promising for valleytronics.

It is found that Δ_V is always significantly greater than Δ_C. These differences rely on distinct orbital contributions. We take the SMoSiN$_2$ and the SCrSiN$_2$ monolayers for comparison to discuss in details. The valence band valleys of the SMoSiN$_2$ (SCrSiN$_2$) monolayer are dominated by $d_{x^2-y^2}$ and d_{xy} orbitals of Mo (Cr) atoms. Table I lists the electric dipole moment of the SMoSiN$_2$ (SCrSiN$_2$) monolayer. Similar to the MoS$_2$ monolayer, the SMoSiN$_2$ (SCrSiN$_2$) monolayer has in-plane polarization, leading to large spin splitting in the valence band. For the conduction band, however, the valley is
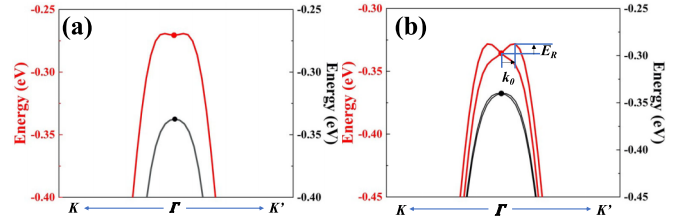
FIG. 6. The magnified valence bands calculated by (a) PBE and (b) PBE+SOC. The red and black lines represent the energy bands of the SeMoSiN$_2$ and the SMoSiN$_2$ monolayers, respectively.

mainly contributed by the d_{z^2} orbital of the Mo (Cr) atom. The d_{z^2} orbital exhibits out-of-plane properties, and the electric dipole moment along out-of-plane direction is very low. Consequently, their spin splittings in conduction bands are vary small. This phenomenon resembles the case of the CrSi$_2$N$_4$ monolayer [50]. For the SCrSiN$_2$ monolayer, the optical transition energy at different valleys belonging to different spin components is $\omega_u/\omega_d = 1.12/1.06$ eV. These values are in the range of infrared to visible light energy, allowing practical applications for solar cells in future [51].

D. Rashba spin splitting

The Rashba effect, an interesting physical phenomenon referred to spin-momentum locking, is widely observed in systems with broken inversion symmetry and strong SOC [52]. The Rashba effect provides a wide field of potential applications, such as magnetoelectric and magnetoptical response and nonlinear transport properties. Especially, the Rashba effect enables manipulation of spin through spin-to-charge interconversion and electrically driven spin torque for spintronic applications [53,54]. The Rashba spin splitting is conventionally shifted by a Rashba momentum offset. However, it could be obtained at the surface state or by using a vertical field to break the planar mirror symmetry [55,56]. The 2D Janus materials with intrinsically planar mirror symmetry breaking are viewed as promising candidates to achieve large Rashba spin splitting [14]. Owing to the breaking of planar inversion symmetry relative to the M atomic layer, the Janus XMSiN$_2$ monolayer is expected to exhibit the Rashba spin splitting. The magnified valence bands are shown in Figs. 6 and S2. The Rashba splitting is dependent on the strength of SOC, the SeMoSiN$_2$ monolayer therefore exhibits prominent Rashba splitting around the Γ point, as shown in Fig. 6(b).

In particular, the strength of the Rashba effect can be examined by three key parameters [57]: Rashba energy E_R, Rashba momentum offset k_0, and Rashba constant α_R. The Rashba constant α_R can be obtained by $\alpha_R = \frac{2E_R}{k_0}$. The corresponding values of the SeMoSiN$_2$ monolayer are $E_R = 7.446$ meV, $k_0 = 0.107$ Å^{-1}, and $\alpha_R = 139$ meVÅ, respectively. The Rashba splitting obtained for the SeMoSiN$_2$ monolayer is significantly larger than that in the WSiGeN$_4$ monolayer [7], which is attributed to the stronger asymmetry in the former case. Recent calculations of Janus SWGeN$_2$ and SeWGeN$_2$ monolayers performed by Vu et al. reported $E_R = 15$–16 meV and a larger value of $\alpha_R \sim 360$ meV Å [58] because of the heavy metal element W. Previous calculation reported a
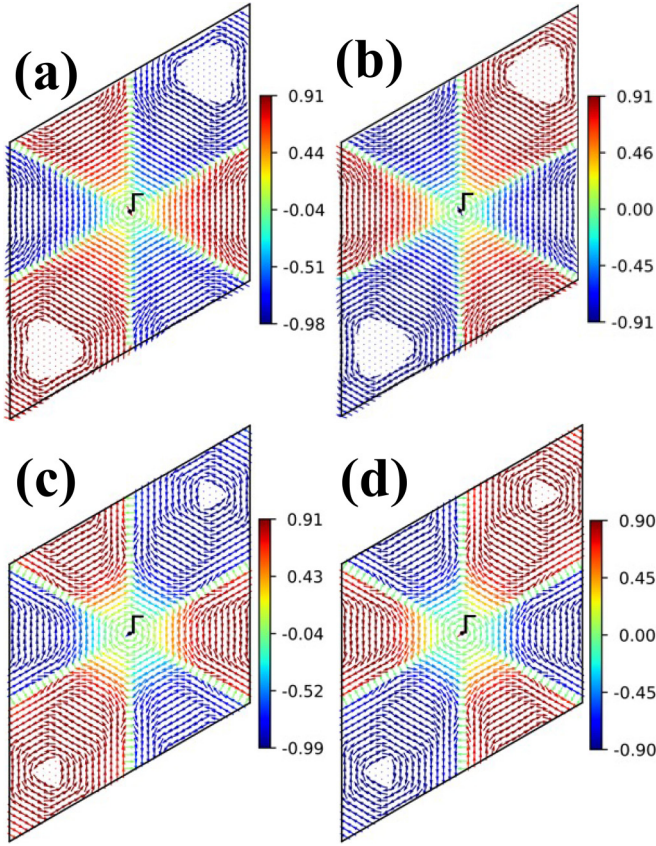
FIG. 7. The spin textures of the (a) second highest occupied state and (b) highest occupied state for the monolayered $SMoSiN_2$. The spin textures of the (c) second highest and (d) highest occupied states for the SeMoSiN$_2$ monolayer. The arrow represents the in-plane component of spin polarization, and the color represents the out-of-plane component of spin polarization, i.e., red (blue) is spin-up (spin-down).

FIG. 8. The band structures of the $SMoSiN_2$ monolayer under different strains and SOC is included in the calculation.

tremendous Rashba parameter of $\alpha_R = 0.92$ eV Å in the WSeTe monolayer relying on large SOC effect introduced by heavy elements [59]. Noticeably, a recent investigation reported the absence of Rashba splitting at the Γ point for the WA_2Z_4 (A = Si or Ge; Z=N, P, or As) monolayers, and a Rashba splitting of $\alpha_R = 120$ meVÅ is anticipated to be achieved by using a 0.5 V/Å vertical electric field [56]. The Janus 2D semiconductors, consisting of strong crystal lattice asymmetry and heavy elements with large SOC, provide great possibilities to achieve large Rashba splitting.

The spin textures shown in Fig. 7 reveal that the second highest and the highest occupied states only have in-plane spin components around the Γ point, and their directions are completely opposite, namely, clockwise and counterclockwise directions. Moreover, the maximal values of the in-plane spin components are obtained at the K/K' valleys. Compared Fig. 7(a) with Fig. 7(b), it is found that the in-plane spin components are fully opposite in the whole BZ. In contrast, the in-plane spin components essentially vanish for the WSi$_2$N$_4$ monolayer [56], which is ascribed to the protection of planar mirror symmetry. Except for the in-plane spin components, Fig. 7(a) shows that spin-up and spin-down components are located at the K and K' valleys, respectively; whereas Fig. 7(b)

shows the exactly opposite results. This is consistent with the spin polarized and valley-spin locked electronic states shown in Fig. 3(c). The spin textures schematically demonstrate strong spin polarization and valley-spin coupling for both $SMoSiN_2$ and SeMoSiN$_2$ monolayers. It is noticed that our calculated spin textures are in good agreement with previous report regarding to the Janus MoSiGeN$_4$ and WSiGeN$_4$ monolayers without planar mirror symmetry [7], and the spin splitting is more prominent in our case.

E. Strain effects

We further investigate the effect of in-plane biaxial strains on the valley-related properties of the $SMoSiN_2$ and SCrSiN$_2$ monolayers. Here, the in-plane strain is defined as

$$\varepsilon = \left(\frac{a - a_0}{a_0} \right) \times 100\%, \tag{4}$$

where a_0 and a represent the lattice constants of 2D monolayer without and with in-plane strains, respectively.

The strain-dependent electronic bands of the $SMoSiN_2$ monolayer are shown in Fig. 8. And the related electronic band structures of the SeMoSiN$_2$ monolayer are shown in Fig. S3. The valley spin splitting of the $SMoSiN_2$ and the SeMoSiN$_2$ monolayers could be substantially modulated by in-plain strains. For the $SMoSiN_2$ monolayer, it is interesting to find that the valley-related spin splitting at the conduction band (Δ_C) almost disappears when a compressive strain of -2% is applied, as evidenced by Fig. 8. This is attributed to the shift of its bottommost conduction band away from the K/K' valleys in the k space. Similar result is also obtained for the MoSi$_2$As$_4$, in which a 4% strain leads to the disappearance of valley at the topmost valence band [4]. Furthermore, the in-plane strain dependent spin splittings and optical transition energies are summarized in Fig. 8.

When the in-plane strain is changed from -2% to 6%, the conduction band spin splitting Δ_C of the $SMoSiN_2$ almost monotonically increases from 2.8 to 5.0 meV. Moreover, its valence band spin splitting Δ_V is substantially enhanced from 103 to 144 meV when the strain is varied from -6% to 6%. It can be seen that Δ_V is an excellent strain-tunable parameter, while Δ_C is insensitive to strain. This feature is
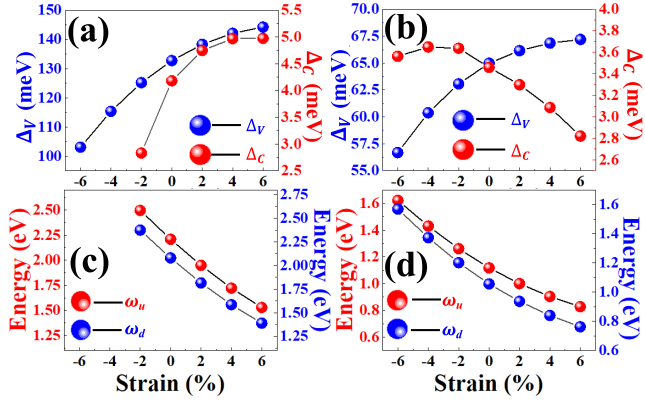
FIG. 9. The valley-related spin splitting, which is calculated by Eq. (2), as a function of in-plane strains for (a) the $SMoSiN_2$ and (b) the $SCrSiN_2$ monolayers. The optical transition energies (ω_u and ω_d), as schematically shown in Fig. 3(c), of the (c) $SMoSiN_2$ and the (d) $SCrSiN_2$ monolayers varied by strains.

FIG. 10. The spin projected band structures of [(a) and (b)] $SMoSiN_2$ and [(c) and (d)] $SCrSiN_2$ monolayers under certain tensile strains with SOC. The color bar represents the weight of the spin component S_z, and red (blue) is spin-up (spin-down).

also observed for $MoSi_2As_4$ and $MoSi_2P_4$ monolayers [48]. In analogy to the $SMoSiN_2$ monolayer, the valence band spin splitting Δ_V of the $SCrSiN_2$ monolayer monotonically increase from 57 to 67 meV when the strain is changed from -6% to 6%. However, its Δ_C is gradually reduced from 3.6 to 2.8 meV, as shown in Fig. 9(b). As schematically shown in Fig. 3(c), ω_u and ω_d are the minimal optical transition energies required for the K valley coupled with spin-up and spin-down components, respectively. Our calculated results shown in Figs. 9(c) and 9(d) reveal that both ω_u and ω_d are gradually reduced when the in-plain strain is changed from compressive strain to tensile strain. This is attributed to the more prominent enhancement of Δ_V and strain insensitivity of Δ_C. Moreover, taken the HSE06 functional correction of about 0.55 eV compared to the GGA-PBE functional into account, the strain-dependent optical transition energies (ω_u and ω_d) are in the range of visible light, indicating potential application of the Janus XMSiN$_2$ for optoelectronics and solar cells [33]. The optical transition difference ω_Δ is calculated by $\omega_\Delta = \omega_u - \omega_d$. It suggests the separation energy between A and B excitons [60]. For the $SMoSiN_2$ monolayer, the in-plane strains give rise to enhanced ω_Δ from 122 to 139 meV, as shown in Fig. S4. The ω_Δ of the $SCrSiN_2$ monolayer is also improved from 52 to 64 meV when strain is changed from -6% to 6%. The significant enhancement of ω_Δ obtained in the $SMoSiN_2$ monolayer indicates that exciton separation energy can be effectively tuned by in-plane strains.

In addition, the spin projected band structures shown in Fig. 10 unveil that valley-spin coupling and complete spin polarization are well preserved regardless of tensile strains. Our calculations suggest the robustness of valley-spin coupling to strain and tunable valley-related spin splitting for the Janus XMSiN$_2$ monolayer.

The optical absorption characteristics of the $SMoSiN_2$ and the $SCrSiN_2$ monolayers are shown in Figs. 11 and S5. The corresponding result of the $MoSi_2N_4$ monolayer is also shown in Fig. 11(a) for comparison. The striking absorption peak is located at about 1 eV for the $SCrSiN_2$ monolayer due to its small electronic band gap. Both $SMoSiN_2$ and $MoSi_2N_4$
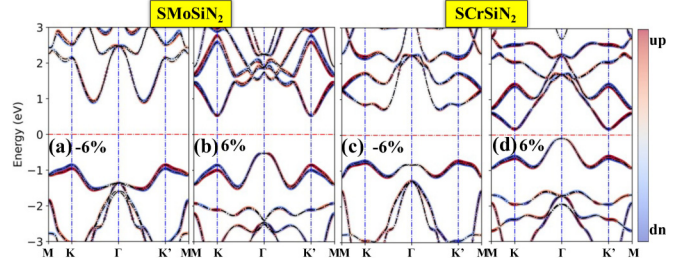
monolayers exhibit distinct absorption at about 2 eV. More importantly, the $SMoSiN_2$ monolayer possesses superior absorption of visible and ultraviolet light to that of the $MoSi_2N_4$ monolayer. The visible light absorptions of the $SCrSiN_2$ and the $SMoSiN_2$ monolayers are significantly stronger than that of the $MoSi_2N_4$ monolayer.

Figures 11(b) and S5 reveal that the optical absorption properties of the $SMoSiN_2$ ($SCrSiN_2$) monolayer are substantially influenced by in-plane strains, demonstrating excellent manipulation of optical absorption features via strain engineering. Specifically, when the in-plane strain is increased from -2% to 6%, the absorption edges of both $SMoSiN_2$ and $SCrSiN_2$ monolayers exhibit significant redshift, which are consistent with the corresponding band-gap variations. Therefore both $SMoSiN_2$ and $SCrSiN_2$ monolayers are expected to be promising candidates for optoelectronic devices.

F. Berry curvature and valleytronics

In addition to opposite spin polarizations, the electronic states of 2D semiconductor at the K/K' valleys have opposite Berry curvatures $\Omega_z(k)$ due to inversion symmetry breaking. It can be calculated by

$$\Omega_z(k) = -\sum_n \sum_{n \neq n'} f_n \frac{2 \operatorname{Im}\langle \psi_{nk} | v_x | \psi_{n'k} \rangle \langle \psi_{n'k} | v_y | \psi_{nk} \rangle}{(E_n - E_n')^2}, \quad (5)$$

where υ are the velocity operator, f_n is the equilibrium Fermi Dirac distribution function; ψ_{nk} is a Bloch wave function with eigenvalue E_n [61,62]. Here, the summation is over all occupied bands.
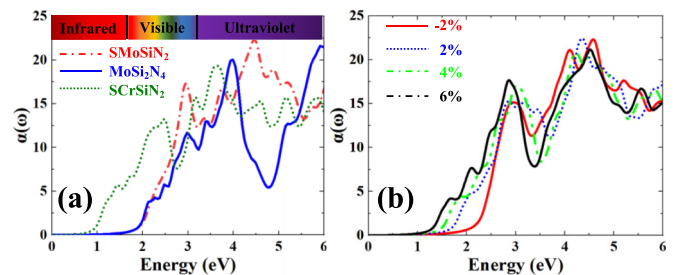
FIG. 11. Optical absorption of (a) the $SMoSiN_2$, $SCrSiN_2$, and $MoSi_2N_4$ monolayers. Optical absorption of (b) the $SMoSiN_2$ monolayer under different in-plane strains.
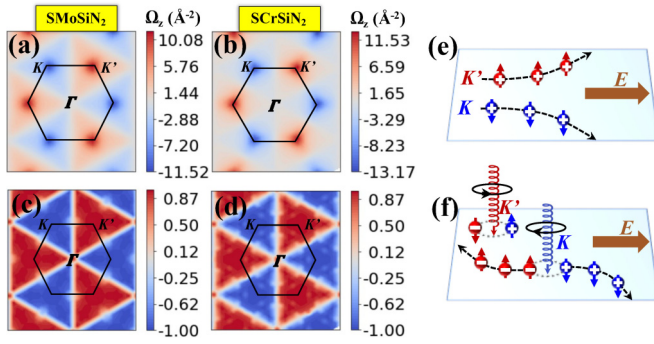
FIG. 12. The Berry curvature distribution for (a) the SMoSiN$_2$ and (b) the SCrSiN$_2$ monolayer, respectively. The contributions from all valence bands are considered. The circular polarizations of (c) the SMoSiN$_2$ and (d) the SCrSiN$_2$ monolayers, respectively. (e) The spin and valley Hall effect diagram of hole-doped SMoSiN$_2$ and SCrSiN$_2$ monolayers. The blue/red sphere represents the hole in the K/K' valley, respectively, and the up/down arrow represents spin-up/down, respectively. (f) The spin and valley Hall effect diagram of the SMoSiN$_2$ and the SCrSiN$_2$ monolayers under the illumination of circularly polarized light at a specific frequency. The $\pm$ symbol in the sphere indicates hole/electron carrier.

Figures 12(a), 12(b), 13(a), and 13(b) illustrate that the monolayers of SMoSiN$_2$, SCrSiN$_2$, SeMoSiN$_2$, and SeCrSiN$_2$ have similar Berry curvatures. The valley carrier with z-direction spin polarization will be separated in real space due to spin-valley locking at the K/K' valleys, which is expected to produce spin Hall effect. The nonzero Berry curvature introduces an anomalous velocity to the carrier: $v(k) = -\frac{e}{\hbar}E \times \Omega_z(k)$, where E is the applied electric field [15]. As a result, the holes at the K and the K' valleys would acquire opposite anomalous velocities and move towards opposite boundaries, as shown in Fig. 12(e). The valley Hall effect indicates that the valley can be treated as a novel
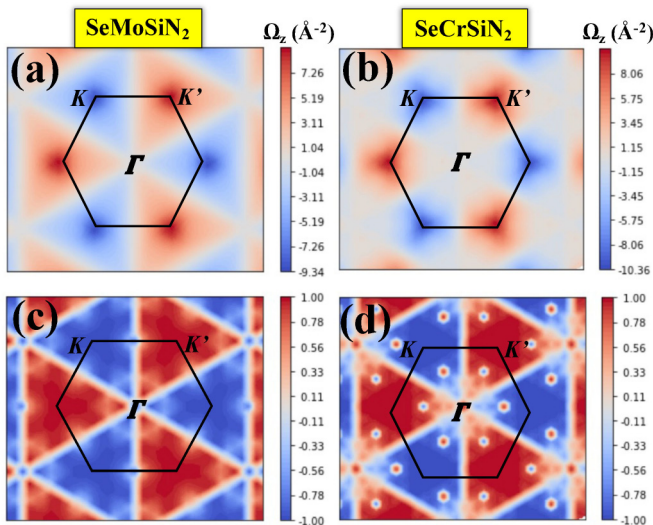
FIG. 13. The Berry curvature Ω_Z distributions for the (a) SeMoSiN$_2$ and (b) SeCrSiN$_2$ monolayers with all valence bands are included, respectively. The circular polarization of the monolayered (c) SeMoSiN$_2$ and (d) SeCrSiN$_2$, respectively.
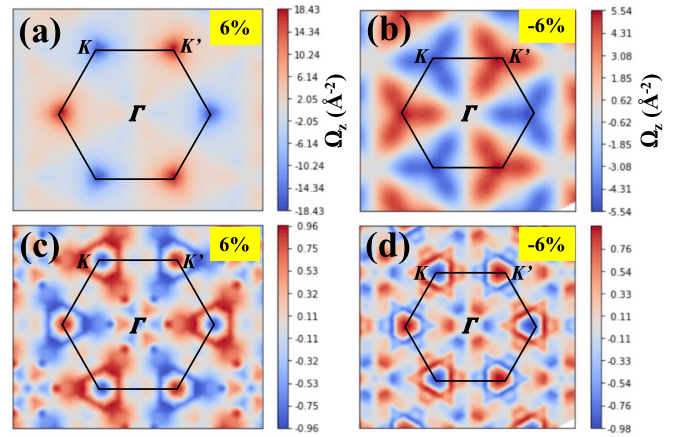
FIG. 14. The distribution of the Berry curvature Ω_Z in the whole BZ for the strained SMoSiN$_2$ monolayer with (a) 6% and (b) −6% in-plane biaxial strains, respectively. The distribution of circular polarization of SMoSiN$_2$ monolayer in the whole BZ under in-plane strains of (c) 6% and (d) −6%.

degree of freedom to encode information. Most importantly, the valley Hall effect allows completely electrical control of valley-related carrier transport, which is crucial to practical applications for valleytronics [63].

Furthermore, the nonzero Berry curvature indicates that the K/K' valley has chirality, which can be described by the selection rule of circularly polarized light. The circular polarization $\eta(\boldsymbol{k})$ is defined as

$$\eta(\boldsymbol{k}) = \frac{|P_+(\boldsymbol{k})|^2 - |P_-(\boldsymbol{k})|^2}{|P_+(\boldsymbol{k})|^2 + |P_-(\boldsymbol{k})|^2}, \tag{6}$$

where $P_\pm(\boldsymbol{k}) = \langle ck|p_x \pm ip_y|vk\rangle$ is the interband transition matrix, which describes the vertical transitions of electrons at point $\boldsymbol{k}$ from the valence band (v) to the conduction band (c) under the radiation fields of left-hand and right-hand circular polarization, respectively [64]. Here, $\eta(\mathbf{k})$ is an optical transition between the highest valence band and the lowest conduction band in Brillouin zone. It is noticed that these transitions take place at different optical frequencies. Figures 12(c), 12(d), 13(c), and 13(d) demonstrate that the lowest transition frequency occurs at the two valleys, and the $\eta(\boldsymbol{k})$ have opposite signs. This calculated result is similar to the situation in the monolayered MoS$_2$ [22]. Therefore the valley Hall effect is anticipated to be achieved in the XMSiN$_2$ monolayer via optical pumping, as shown in the Fig. 12(f). The carriers are selectively stimulated by circularly polarized light, and the photoexcited electron-hole pair is valley-dependent and spin-dependent. The spin-valley coupling combined with optical selection rule can be utilized to generate pure spin current on the opposite sides, which is favorable for developing spintronic devices [65]. More recently, various van der Waals (vdW) heterostructures are constructed to manipulate the valley-dependent exciton transport via modulating twist angle [66].

The in-plane biaxial strains also could tune the Berry curvature, as evidenced by Figs. 14(a) and 14(b). More importantly, we can straightforwardly convince that the Berry curvature is remarkably enhanced by using 6% tensile strain,
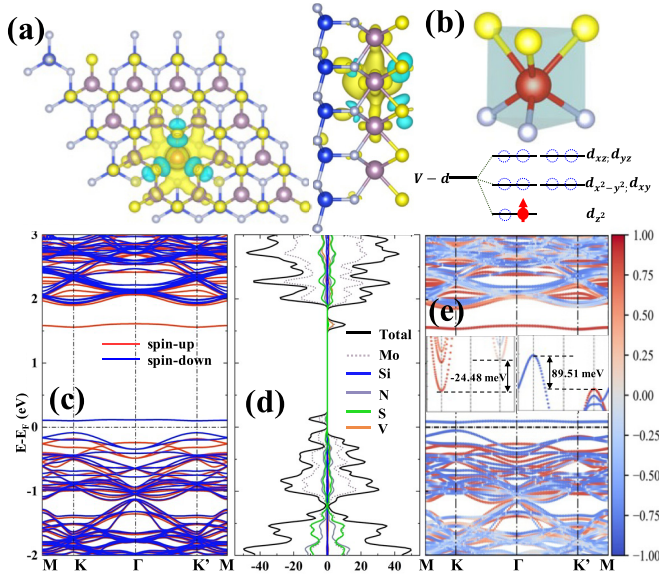
FIG. 15. (a) The V-doped SMoSiN$_2$ monolayer. The yellow and green isosurfaces represent spin up and spin down charges, respectively. The isosurface value is set to 0.01 e/Å^3. (b) The splitting of d orbitals for the V atom owing to the trigonal prismatic crystal field. (c) The band structure and (d) orbital-projected density of states of the V-doped SMoSiN$_2$ monolayers without SOC. The red and blue lines represent spin-up and spin-down components, respectively. (e) The band structure of the V-doped SMoSiN$_2$ monolayer with SOC. The inset shows the amplified details of the conduction (left) and valence (right) bands at the K/K' valleys, respectively.

as verified by the maximal values of the Ω_Z distribution shown in Fig. 14(a). The Ω_Z is almost reduced to half when a -6% compressive strain is implemented. The time reversal symmetry protects the Berry curvatures at the K/K' valleys possessing completely opposite values. It is also an indication of valley-spin coupling, which is in accordance with the result shown in Fig. 10(a). Hence, the completely polarized Berry curvatures at the K/K' valleys are preserved when -6% strain is performed. However, the Berry curvature extremal positions in the k space is not only concentrated at the K/K' valleys, as visualized in Fig. 14(b). The in-plane strains do not significantly modify the circularly polarized polarization at the K/K' valleys, as shown in Figs. 13(c) and 13(d). The coexistence of spin and valley Hall effects and effective tuning of XMSiN$_2$ monolayers via strain engineering are beneficial for their practical applications for valleytronics.

G. Effects of V doping on valley polarization

Furthermore, we examine time reversal symmetry breaking by introducing magnetic moment to enhance valley polarization. Generally, ferromagnetic substrate could induce valley splitting of about tens of meV originated from proximity effect [67,68]. Compared to the magnetic proximity effect, substitutional doping always give rise to larger valley splitting [48]. Most importantly, previous experimental studies have shown that transition metal atoms, such as Fe, V, can be used as dopants to introduce magnetism into 2D TMDs [69,70]. As shown in Fig. 15(a), we construct a

$4 \times 4 \times 1$ SMoSiN$_2$ supercell and replace one Mo atom with one V atom (doping concentration is 6.25%).

The substitutional V atom forms trigonal prismatic crystal field, as evidenced by Fig. 15(b), leading to the splitting of the d orbitals into three categories: one a orbital (d_{z^2}), two e_1 orbitals (d_{xy} and $d_{x^2-y^2}$), and two e_2 orbitals (d_{xz} and d_{yz}) [71]. The V atom is chemically bonded with the neighboring three S atoms and three N atoms to donate four valence electron. As a consequence, V^{4+} is generated with electron configuration of $a_1 e_1^0 e_2^0$. According to theoretical analysis, the V-doped SMoSiN$_2$ monolayer is expected to be spin polarized with a total magnetic moment of about 1.0 μ_B for each V substitutional doping, and magnetic moment is contributed by the d_{z^2} orbital. This is further confirmed from the spin density of the V-doped SMoSiN$_2$. Our calculations reveal that the magnetic moment is mainly located at the V atom with approximately 0.64 μ_B, and the nearest neighboring atoms hold relatively small and opposite magnetic moments, as described in details in Fig. S6. It suggests that the V atom is weakly antiferromagnetic coupled with the S atoms. Moreover, the first nearest neighboring Mo atoms are found to possess distinct magnetic moments, manifesting strong interaction between the V atom and the Mo atoms. The emerging strong interaction substantially breaks the time-reversal symmetry of the SMoSiN$_2$ monolayer, leading to a remarkable valley polarization at the K/K' valleys.

The electronic structure of the V-doped SMoSiN$_2$ without SOC is shown in Figs. 15(c) and 15(d). Significant spin splittings between the spin-up and the spin-down components are observed, which is originated from the emergence of the net magnetic moment to lift the spin degeneracy. This is consistent with the observation of strong spin polarization arising from the d_{z^2} orbital of the V atom, as exhibited in the projected density of states in Fig. S6. Compared with the pristine SMoSiN$_2$ monolayer, the V atom impurity would introduce several defect states in its band gap. Two defect states, one is located slightly above the Fermi level and the other one is 1.5 eV higher than the Fermi level, are dominated by Mo, V, and N atoms. Apart from the presence of the defect states in the band gap, the main features of the valley-related properties are preserved. In particular, the K/K' valleys of the V-doped SMoSiN$_2$ monolayer remains degenerate when the SOC effect is not included. However, when the SOC effect is taken into account, the energy degeneracy at the K/K' valleys are lifted as a result of time reversal symmetry breaking. Specifically, the valley degeneracy at the valence band is substantially destroyed and a giant valley polarization is achieved, as demonstrated in Fig. 15(e). Following previous definition [22], the valley splitting for valence band Δ_{VB} and conduction band Δ_{CB} are defined as

$$\Delta_{VB} = E_K^{VB} - E_{K'}^{VB'} \left(\Delta_{CB} = E_K^{CB} - E_{K'}^{CB'} \right), \qquad (7)$$

where $E_K^{VB}/E_{K'}^{VB'}$ ($E_K^{CB}/E_{K'}^{CB'}$) are the energy extreme values at the K/K' valleys at the valence band (conduction band).

The Δ_{VB} (Δ_{CB}) of the V-doped SMoSiN$_2$ monolayer is 89.51 meV (-24.48 meV) when SOC is considered. The distinct discrepancies between Δ_{VB} and Δ_{VB} stem from different orbital characters. Based on tight binding model demonstrated previously [22,71], the $d_{xy}/d_{x^2-y^2}$ orbital could induce

large valley polarization due to the C_3 symmetry, while the d_{z^2} orbital do not induce valley polarization. As presented in Fig. S6(d), the VBM is completely contributed by the $d_{xy}/d_{x^2-y^2}$ orbital of the V atom, and the d_{z^2} orbital mainly governs the CBM. However, the $d_{xy}/d_{x^2-y^2}$ orbital also has considerable contributions to the CBM at the K' valley. Thus our calculated Δ_{VB} and Δ_{CB} values agree well with expectation. It is noticed that the calculated Δ_{VB} of 89.51 meV is remarkably larger than the reported value in the V-doped $MoSi_2As_4$ (25 meV) or V-doped $MoSi_2P_4$ (34 meV) [48]. A recent theoretical work relevant to the V doping in the $SMoSiN_2$ monolayer reported a similar result (64 meV), and the Cr doping could introduce a larger valley splitting in valence band (89 meV) due to the localization of the $3d$ orbital compared to the $4d$ orbital [72]. However, the valence band energy extreme point is not located at the K valley for the Cr-doped $SMoSiN_2$ monolayer. Based on the Hund's rule and Pauli exclusion principle, substitutional dopings of Mn and Fe and Co in the Janus $XMSiN_2$ monolayer are anticipated to generate more prominent valley polarization. It is interesting to find that the valley splitting in the V-doped $SMoSiN_2$ monolayer is almost comparable with the reported values of about 76 meV in Co-doped WTe_2 monolayer [73] and 83.3 meV in the $MoTe_2/MnSe_2$ heterostructure [74]. The large valley splitting value in the V-doped $SMoSiN_2$ monolayer is favorable for developing valley-related nanodevice, which is equivalent to applying a magnetic field of about 570–1140 T to achieve Zeeman valley splitting [75]. Experimental researches have demonstrated that the valley splittings in the MoS_2 monolayer could be generated by Fe and Co substitutional dopings, and valley splitting magnitudes are proportional to the doping concentration [69,76]. The enhanced valley splitting and spin-valley polarization are experimentally observed in chemical vapor deposition (CVD) grown MoS_2 monolayer resulted from defect-bound excitons [77]. These experimental techniques pave the way to manipulate the valley splitting in various 2D semiconductors. Since magnetic atom doping has been successfully realized by direct vapor transport and pulsed laser deposition [78,79], we thus believe that the V-doped $SMoSiN_2$ monolayer is experimentally feasible and is a promising candidate for valleytronics.

Nevertheless, some shortcomings are probably introduced via magnetic atom doping, such as the reduced carrier transport by the surface cluster stimulated by magnetic doping. Another issue arising from the magnetic atom doping is the Curie temperature of the system could be significantly altered by substitutional doping [80]. To achieve a sizable and tunable valley polarization for room temperature application, the exploration of various 2D semiconductor candidates with spontaneous ferromagnetism is still a challenging task. Fortunately, some alternative methods are proposed and experimentally verified, such as the creation of vdW heterostructure with 2D ferromagnetic substrate for manipulating

spin splitting [81–83] and the optically controlled valley via light-valley interaction [43]. Recent studies have proposed some promising 2D materials, such as $FeCl_2$, VGe_2P_4, and RuClBr monolayers, and they are demonstrated to exhibit 2D magnets and strain-driven nontrivial topological phases [84–86]. These 2D materials are expected to be excellent components for spintronic and valleytronic devices [87].

The Janus $XMSiN_2$ monolayers are shown to possess excellent dynamical stability and some unique properties due to their broken planar inversion symmetry, offering many potential application areas for emergent spintronic device, novel quantum device, and energy conversion device. The 2D Janus $XMSiN_2$ monolayers with strong absorption of visible light could offer some competitive candidates for solar cells. Moreover, the built-in polarization field in the 2D Janus $XMSiN_2$ monolayers arising from the inversion symmetry breaking is likely to facilitate photoexcited carrier separation as well as make piezoelectric device. Compared to the tremendous progress from theoretical predictions, the experimental fabrication of various 2D Janus materials is still in infancy. It is expected to gain more comprehensive and physical understandings relevant to the 2D Janus materials once their fabrications are experimentally accessible and reproducible.

IV. CONCLUSIONS

In conclusion, we demonstrate that the Janus $XMSiN_2$ monolayer is a promising 2D valleytronic material. The valley-related spin splittings are obtained in the valleys of the conduction and valence bands due to the intrinsic inversion symmetry breaking and SOC effect. The strong crystal lattice asymmetry and heavy metal elements in the Janus $SeMoSiN_2$ monolayer lead to prominent Rashba spin splitting at the Γ point. The valley and spin Hall effects are proposed to be achievable in the $XMSiN_2$ monolayer with the opposite Berry curvatures at the K/K' valleys. The in-plane biaxial strains could effectively tune the spin splitting, optical absorption and Berry curvature of the $XMSiN_2$ monolayer, allowing its potential application for spintronic and valleytronic devices. Most importantly, our calculation predicates that a giant valley polarization in the $XMSiN_2$ monolayer can be achieved by V atom substitutional doping. Our findings provide a novel computational design based on Janus $XMSiN_2$ monolayer, which could broaden 2D valleytronic semiconductor family for practical applications.

ACKNOWLEDGMENTS

[1] F. Liang, C. Zhang, and Z. Yang, Adv. Mater. **26**, 6944 (2014).

[2] R. Li, Y. Cheng, and W. Huang, Small **14**, 1802091 (2018).

[3] M. Yagmurcukardes, Y. Mogulkoc, B. Akgenc, A. Mogulkoc, and F. M. Peeters, Phys. Rev. B **104**, 045425 (2021).

[4] S. Li, W. Wu, X. Feng, S. Guan, W. Feng, Y. Yao, and S. A. Yang, Phys. Rev. B **102**, 235435 (2020).

[5] T. Hu, F. Jia, G. Zhao, J. Wu, A. Stroppa, and W. Ren, Phys. Rev. B **97**, 235404 (2018).

[6] L. Zhang, Z. Yang, T. Gong, R. Pan, H. Wang, Z. Guo, H. Zhang, and X. Fu, J. Mater. Chem. A **8**, 8813 (2020).

[7] S.-D. Guo, W.-Q. Mu, Y.-T. Zhu, R.-Y. Han, and W.-C. Ren, J. Mater. Chem. C **9**, 2464 (2021).

[8] S. B. Touski and N. Ghobadi, Phys. Rev. B **103**, 165404 (2021).

[9] L. Dong, J. Lou, and V. B. Shenoy, ACS Nano **11**, 8242 (2017).

[10] W. Shi, G. Li, and Z. Wang, J. Phys. Chem. C **123**, 12261 (2019).

[11] C. Tan, Z. Luo, A. Chaturvedi, Y. Cai, Y. Du, Y. Gong, Y. Huang, Z. Lai, X. Zhang, L. Zheng, X. Qi, M. H. Goh, J. Wang, S. Han, X.-J. Wu, L. Gu, C. Kloc, and H. Zhang, Adv. Mater. **30**, 1705509 (2018).

[12] J. R. Schaibley, H. Yu, G. Clark, P. Rivera, J. S. Ross, K. L. Seyler, W. Yao, and X. Xu, Nat. Rev. Mater. **1**, 16055 (2016).

[13] S. A. Vitale, D. Nezich, J. O. Varghese, P. Kim, N. Gedik, P. Jarillo-Herrero, D. Xiao, and M. Rothschild, Small **14**, 1801483 (2018).

[14] M. Yagmurcukardes, Y. Qin, S. Ozen, M. Sayyad, F. M. Peeters, S. Tongay, and H. Sahin, Appl. Phys. Rev. **7**, 011311 (2020).

[15] D. Xiao, W. Yao, and Q. Niu, Phys. Rev. Lett. **99**, 236809 (2007).

[16] O. Gunawan, Y. P. Shkolnikov, K. Vakili, T. Gokmen, E. P. De Poortere, and M. Shayegan, Phys. Rev. Lett. **97**, 186404 (2006).

[17] S.-D. Guo, W.-Q. Mu, J.-H. Wang, Y.-X. Yang, B. Wang, and Y.-S. Ang, Phys. Rev. B **106**, 064416 (2022).

[18] P. Liu, S. Liu, M. Jia, H. Yin, G. Zhang, F. Ren, B. Wang, and C. Liu, Appl. Phys. Lett. **121**, 063103 (2022).

[19] M.-Y. Liu, Y. He, X. Li, and K. Xiong, Phys. Chem. Chem. Phys. **25**, 7278 (2023).

[20] S. Sheoran, A. Phutela, R. Moulik, and S. Bhattacharya, J. Phys. Chem. C **127**, 11396 (2023).

[21] Z. Y. Zhu, Y. C. Cheng, and U. Schwingenschloegl, Phys. Rev. B **84**, 153402 (2011).

[22] D. Xiao, G.-B. Liu, W. Feng, X. Xu, and W. Yao, Phys. Rev. Lett. **108**, 196802 (2012).

[23] X. Qian, J. Liu, L. Fu, and J. Li, Science **346**, 1344 (2014).

[24] K. F. Mak, K. L. McGill, J. Park, and P. L. McEuen, Science **344**, 1489 (2014).

[25] J. Zhao, X. Jin, H. Zeng, C. Yao, and G. Yan, Appl. Phys. Lett. **119**, 213101 (2021).

[26] R. T. Sibatov, R. M. Meftakhutdinov, and A. I. Kochaev, Appl. Surf. Sci. **585**, 152465 (2022).

[27] P. T. L. Tran, N. V. Hieu, H. Bui D, Q. N. Cuong, and N. N. Hieu, Nanoscale Adv. **5**, 3104 (2023).

[28] S.-T. Nguyen, P. V. Cuong, N. Q. Cuong, and C. V. Nguyen, Dalton Trans. **51**, 14338 (2022).

[29] S.-T. Nguyen, C. Q. Nguyen, Y. S. Ang, H. V. Phuc, N. N. Hieu, N. T. Hiep, N. M. Hung, L. T. T. Phuong, N. V. Hieu, and C. V. Nguyen, J. Phys. D: Appl. Phys. **56**, 045306 (2023).

[30] J. Zhao, H. Zeng, and X. Zhou, Carbon **145**, 1 (2019).

[31] Y. Feng, Z. Wang, X. Zuo, and G. Gao, Appl. Phys. Lett. **120**, 092405 (2022).

[32] Y.-L. Hong, Z. Liu, L. Wang, T. Zhou, W. Ma, C. Xu, S. Feng, L. Chen, M.-L. Chen, D.-M. Sun, X.-Q. Chen, H.-M. Cheng, and W. Ren, Science **369**, 670 (2020).

[33] Y. Yin, Q. Gong, M. Yi, and W. Guo, Adv. Funct. Mater. **33**, 2214050 (2023).

[34] G. Kresse and J. J. Furthmüller, Phys. Rev. B **54**, 11169 (1996).

[35] P. E. Blöchl, Phys. Rev. B **50**, 17953 (1994).

[36] J. P. Perdew, K. Burke, and M. Ernzerhof, Phys. Rev. Lett. **77**, 3865(E) (1996).

[37] H. J. Monkhorst and J. D. Pack, Phys. Rev. B **13**, 5188 (1976).

[38] M. Gajdoš, K. Hummer, G. Kresse, J. Furthmüller, and F. Bechstedt, Phys. Rev. B **73**, 045112 (2006).

[39] A. Togo and I. Tanaka, Scr. Mater. **108**, 1 (2015).

[40] U. Herath, P. Tavadze, X. He, E. Bousquet, S. Singh, F. Munoz, and A. H. Romero, Comput. Phys. Commun. **251**, 107080 (2020).

[41] S.-W. Kim, H.-J. Kim, S. Cheon, and T.-H. Kim, Phys. Rev. Lett. **128**, 046401 (2022).

[42] V. Wang, N. Xu, J.-C. Liu, G. Tang, and W.-T. Geng, Comput. Phys. Commun. **267**, 108033 (2021).

[43] K. F. Mak, D. Xiao, and J. Shan, Nat. Photon. **12**, 451 (2018).

[44] J. Heyd, G. E. Scuseria, and M. Ernzerhof, J. Chem. Phys. **118**, 8207 (2003).

[45] See Supplemental Material at http://link.aps.org/supplemental/10.1103/PhysRevB.109.035408 for the band structures of the SMoSiN$_2$ and the SCrSiN$_2$ monolayers calculated by HSE06 without SOC. The magnified valence bands around the Fermi level to show the Rashba-type spin splitting for the monolayered SCrSiN$_2$ and SeCrSiN$_2$. The band structure of SCrSiN$_2$ with SOC under different strains. The strain dependent optical transition difference for the SMoSiN$_2$ and SCrSiN$_2$ monolayers. Optical absorption of the SCrSiN$_2$ monolayer under different in-plane strains. The V-doping in the SMoSiN$_2$ monolayer, including the magnetic moments at some atoms and the projected density of states of the V atom and the V-atom orbital-resolved band structure with SOC effect.

[46] J. Yuan, Q. Wei, M. Sun, X. Yan, Y. Cai, L. Shen, and U. Schwingenschlögl, Phys. Rev. B **105**, 195151 (2022).

[47] A. Kormányos, V. Zólyomi, N. D. Drummond, P. Rakyta, G. Burkard, and V. I. Fal'ko, Phys. Rev. B **88**, 045416 (2013).

[48] H. Ai, D. Liu, J. Geng, S. Wang, K. H. Lo, and H. Pan, Phys. Chem. Chem. Phys. **23**, 3144 (2021).

[49] Y. Li, M. Lan, S. Wang, T. Huang, Y. Chen, H. Wu, F. Li, and Y. Pu, Phys. Chem. Chem. Phys. **25**, 15676 (2023).

[50] Y. Liu, T. Zhang, K. Dou, W. Du, R. Peng, Y. Dai, B. Huang, and Y. Ma, J. Phys. Chem. Lett. **12**, 8341 (2021).

[51] L. Zhang, H. Zeng, Z. Fan, and D.-Z. Ding, IEEE J. Multiscale Multiphysics Comput. Tech. **8**, 71 (2023).

[52] G. Bihlmayer, P. Noël, D. V. Vyalikh, E. V. Chulkov, and A. Manchon, Nat. Rev. Phys. **4**, 642 (2022).

[53] I. M. Miron, G. Gaudin, S. Auffret, B. Rodmacq, A. Schuhl, S. Pizzini, J. Vogel, and P. Gambardella, Nat. Mater. **9**, 230 (2010).

[54] A. Manchon, J. Železný, I. M. Miron, T. Jungwirth, J. Sinova, A. Thiaville, K. Garello, and P. Gambardella, Rev. Mod. Phys. **91**, 035004 (2019).

[55] K. Ishizaka, M. S. Bahramy, H. Murakawa, M. Sakano, T. Shimojima, T. Sonobe, K. Koizumi, S. Shin, H. Miyahara, A. Kimura, K. Miyamoto, T. Okuda, H. Namatame, M. Taniguchi, R. Arita, N. Nagaosa, K. Kobayashi, Y. Murakami, R. Kumai, Y. Kaneko *et al.*, Nat. Mater. **10**, 521 (2011).

[56] S. Sheoran, S. Monga, A. Phutela, and S. Bhattacharya, J. Phys. Chem. Lett. **14**, 1494 (2023).

[57] J. Zhao, W. Guo, and J. Ma, Nano Res. **10**, 491 (2017).

[58] T. V. Vu, H. V. Phuc, C. V. Nguyen, V. T. T. Vi, A. I. Kartamyshev, and N. N. Hieu, Phys. Chem. Chem. Phys. **24**, 16512 (2022).

[59] Q.-F. Yao, J. Cai, W.-Y. Tong, S.-J. Gong, J.-Q. Wang, X. Wan, C.-G. Duan, and J. H. Chu, Phys. Rev. B **95**, 165401 (2017).

[60] T. Wozniak, U. E. hani, P. E. Faria Jr., M. S. Ramzan, and A. B. Kuc, Small **19**, 2206444 (2023).

[61] C. Ke, Y. Wu, W. Yang, Z. Wu, C. Zhang, X. Li, and J. Kang, Phys. Rev. B **100**, 195435 (2019).

[62] Y. Yao, L. Kleinman, A. H. MacDonald, J. Sinova, T. Jungwirth, D.-S. Wang, E. Wang, and Q. Niu, Phys. Rev. Lett. **92**, 037204 (2004).

[63] J. Yin, C. Tan, D. Barcons-Ruiz, I. Torre, K. Watanabe, T. Taniguchi, J. C. W. Song, J. Hone, and F. H. L. Koppens, Science **375**, 1398 (2022).

[64] T. Cao, G. Wang, W. Han, H. Ye, C. Zhu, J. Shi, Q. Niu, P. Tan, E. Wang, B. Liu, and J. Feng, Nat. Commun. **3**, 887 (2012).

[65] Z. Wu, B. T. Zhou, X. Cai, P. Cheung, G.-B. Liu, M. Huang, J. Lin, T. Han, L. An, Y. Wang, S. Xu, G. Long, C. Cheng, K. T. Law, F. Zhang, and N. Wang, Nat. Commun. **10**, 611 (2019).

[66] D. Unuchek, A. Ciarrocchi, A. Avsar, Z. Sun, K. Watanabe, T. Taniguchi, and A. Kis, Nat. Nanotechnol. **14**, 1104 (2019).

[67] Q. Li, K.-Q. Chen, and L.-M. Tang, Phys. Rev. Appl. **13**, 014064 (2020).

[68] Y. Qi, C. Yao, J. Zhao, and H. Zeng, Phys. Rev. B **108**, 125304 (2023).

[69] Q. Li, X. Zhao, L. Deng, Z. Shi, S. Liu, Q. Wei, L. Zhang, Y. Cheng, L. Zhang, H. Lu, W. Gao, W. Huang, C.-W. Qiu, G. Xiang, S. J. Pennycook, Q. Xiong, K. P. Loh, and B. Peng, ACS Nano **14**, 4636 (2020).

[70] S. Bolar, S. Shit, J. S. Kumar, N. C. Murmu, R. S. Ganesh, H. Inokawa, and T. Kuila, Appl. Catal., B **254**, 432 (2019).

[71] X. Feng, X. Xu, Z. He, R. Peng, Y. Dai, B. Huang, and Y. Ma, Phys. Rev. B **104**, 075421 (2021).

[72] L. Geng, K. Chen, H. Lu, S. Wang, and Y. Yang, Phys. Chem. Chem. Phys. **25**, 32021 (2023).

[73] X. W. Zhao, Y. Li, R. D. Liang, G. C. Hu, X. B. Yuan, and J. F. Ren, Appl. Surf. Sci. **504**, 144367 (2020).

[74] Q. Li, C.-X. Zhang, D. Wang, K.-Q. Chen, and L.-M. Tang, Mater. Adv. **3**, 2927 (2022).

[75] G. Aivazian, Z. Gong, A. M. Jones, R.-L. Chu, J. Yan, D. G. Mandrus, C. Zhang, D. Cobden, W. Yao, and X. Xu, Nat. Phys. **11**, 148 (2015).

[76] J. Zhou, J. Lin, H. Sims, C. Jiang, C. Cong, J. A. Brehm, Z. Zhang, L. Niu, Y. Chen, Y. Zhou, Y. Wang, F. Liu, C. Zhu, T. Yu, K. Suenaga, R. Mishra, S. T. Pantelides, Z.-G. Zhu, W. Gao, Z. Liu *et al.*, Adv. Mater. **32**, 1906536 (2020).

[77] Y. Wang, L. Deng, Q. Wei, Y. Wan, Z. Liu, X. Lu, Y. Li, L. Bi, L. Zhang, H. Lu, H. Chen, P. Zhou, L. Zhang, Y. Cheng, X. Zhao, Y. Ye, W. Huang, S. J. Pennycook, K. P. Loh, and B. Peng, Nano Lett. **20**, 2129 (2020).

[78] B. Li, T. Xing, M. Zhong, L. Huang, N. Lei, J. Zhang, J. Li, and Z. Wei, Nat. Commun. **8**, 1958 (2017).

[79] T. Fukumura, Z.-W. Jin, A. Ohtomo, H. Koinuma, and M. Kawasaki, Appl. Phys. Lett. **75**, 3366 (1999).

[80] S. Tiwari, M. L. Van de Put, B. Sorée, and W. G. Vandenberghe, NPJ 2D Mater. Appl. **5**, 54 (2021).

[81] K. Zollner, P. E. Faria Jr., and J. Fabian, Phys. Rev. B **107**, 035112 (2023).

[82] D. Zhong, K. L. Seyler, X. Linpeng, R. Cheng, N. Sivadas, B. Huang, E. Schmidgall, T. Taniguchi, K. Watanabe, M. A. McGuire, W. Yao, D. Xiao, K.-M. C. Fu, and X. Xu, Sci. Adv. **3**, e1603113 (2017).

[83] J. F. Sierra, J. Fabian, R. K. Kawakami, S. Roche, and S. O. Valenzuela, Nat. Nanotechnol. **16**, 856 (2021).

[84] T. Zhang, X. Xu, B. Huang, Y. Dai, and Y. Ma, npj Comput. Mater. **8**, 64 (2022).

[85] S.-D. Guo, Y.-L. Tao, H.-T. Guo, Z.-Y. Zhao, B. Wang, G. Wang, and X. Wang, Phys. Rev. B **107**, 054414 (2023).

[86] H. Sun, S.-S. Li, W.-X. Ji, and C.-W. Zhang, Phys. Rev. B **105**, 195112 (2022).

[87] C. C. Tho, S.-D. Guo, S.-J. Liang, W. L. Ong, C. S. Lau, L. Cao, G. Wang, and Y. S. Ang, Appl. Phys. Rev. **10**, 041307 (2023).